The 3-5 MHz global reflectivity map of Mars by MARSIS/Mars Express: implications for the current inventory of subsurface HO

J. Mouginot, A. Pommerol, W. Kofman, P. Beck, B. Schmitt, A. Herique, C. Grima, A. Safaeinili, J.J. Plaut

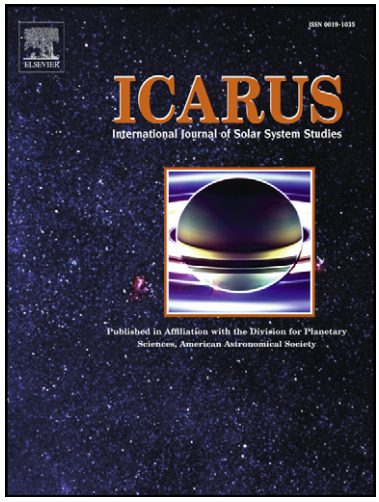

The 3-5 MHz global reflectivity map of Mars by MARSIS/Mars Express: implications for the current inventory of subsurface H_2O

J. Mouginot, A. Pommerol, W. Kofman, P. Beck, B. Schmitt, A. Herique, C. Grima, A. Safaeinili, J.J. Plaut

PII: S0019-1035(10)00275-7
DOI: 10.1016/j.icarus.2010.07.003
Reference: YICAR 9499

To appear in: *Icarus*

Received Date: 5 February 2010
Revised Date: 28 June 2010
Accepted Date: 1 July 2010

Please cite this article as: Mouginot, J., Pommerol, A., Kofman, W., Beck, P., Schmitt, B., Herique, A., Grima, C., Safaeinili, A., Plaut, J.J., The 3-5 MHz global reflectivity map of Mars by MARSIS/Mars Express: implications for the current inventory of subsurface H_2O, *Icarus* (2010), doi: 10.1016/j.icarus.2010.07.003

The 3-5 MHz global reflectivity map of Mars by MARSIS/Mars Express: implications for the current inventory of subsurface H_2O.

J. Mouginot[1,2], A. Pommerol[1,3], W. Kofman[1], P. Beck[1], B. Schmitt[1], A. Herique[1], C. Grima[1], A. Safaeinili[4] and J.J. Plaut[4]

[1]Laboratoire de Planétologie de Grenoble, UJF-Grenoble I/CNRS, France.

[2]University of California Irvine, CA, USA.

[3]Physikalisches Institut, Universitaet Bern, Switzerland.

[4]Jet Propulsion Laboratory, Pasadena, CA, USA.

To be submitted to *Icarus*

40 pages

1 table

10 figures

Abstract

We extracted the surface echo power from two years of MARSIS measurements. The retrieved values are calibrated to compensate for changes in the distance of the spacecraft to the surface and for the attenuation of the signal by the ionosphere. The results are used to build the first global map of surface echo power at 3-5 MHz. The surface echo power variations are primarily caused by km-scale surface roughness. Then, we derive the values of dielectric constant of the shallow subsurface materials by normalizing the surface echo power map using a simulation of MARSIS signal from the MOLA topography. As a result, we obtain a map that characterizes the dielectric properties of the materials down to a few decameters below the surface. Dielectric properties vary with latitude, with high values in mid-latitudes belts (20-40°) and lower values at both equatorial and high latitudes. From the comparison of MARSIS reflectivity map to GRS observations, we conclude that the reflectivity decrease observed poleward of 50-60° corresponds to the onset of water-ice occurrence within the regolith. Assuming homogenous ground composition and texture at the scale of the MARSIS resolution cell, our inferred volume of ground water ice is of 10^6 km^3, equivalent to a polar cap. Low reflectivity areas are also observed in equatorial regions. From radar studies alone, equatorial low dielectric constant values could have different interpretations but the correlation with GRS hydrogen distribution rather points toward a water related explanation.

1. Introduction

The Martian surface has been scrutinized for decades by a variety of imaging and spectroscopic techniques, sensitive to the properties of the first micrometers to millimeters of the surface. Meanwhile, subsurface investigations remained limited to indirect studies until the arrival of the Mars Odyssey mission in 2001. Data from the Gamma Ray Spectrometer (GRS) were used to map the average chemical composition of the first meter below the surface (e.g. Boynton et al., 2007). The spatial distribution of hydrogen (inferred to be present in the form of ground ice) in both hemispheres is one of the major results of this instrument (Boyton et al., 2002; Feldman et al., 2002; Mitrofanov et al., 2002). In order to infer and map the properties of the Martian regolith and crust below this depth of 1 m, "ground penetrating" geophysical techniques are required.

Whereas low frequency radar has been used in the past to probe the subsurface of Mars using terrestrial ground based instruments, the Mars Advanced Radar for Subsurface and Ionospheric Sounding instrument (MARSIS) on board Mars Express (Picardi et al. 2005) was the first radar sounder to operate from an orbiting probe around Mars. It has then been joined by the Shallow Subsurface Radar (SHARAD) on board Mars Reconnaissance Orbiter (Seu et al., 2007). MARSIS is a decameter radar sounder that operates in 1 MHz-wide frequency bands centered at 1.8, 3, 4 and 5 MHz, whereas SHARAD operates at higher frequency (20 MHz) and with a larger bandwidth (10 MHz), which leads to smaller penetration depth but higher vertical resolution. These two instruments measure 2D "radargrams" that represent cross-sections of the Martian subsurface displaying discrete or continuous reflections of the radar waves at interfaces between materials of different dielectric constant (e.g. Plaut

et al. 2007; Watters et al., 2007; Grima et al. 2009). Penetration depth of MARSIS can reach 4 kilometers in clear water ice (Plaut et al. 2007), and this instrument was able to map the bedrock/ice interface below Mars polar caps.

Here, instead of looking at individual radargrams, we build a global map of Mars by extracting the surface echo power from each frame (pulse) of each radargram. This so-called "reflectivity map" gives important information on the composition and physical properties of the upper part of the Martian crust at a global scale. Radar reflectivity maps of the Moon at different frequencies have already been measured in the past from ground-based instruments and used to infer important properties of the Lunar terrains (Evans 1962; Evans and Pettengill 1963). In particular, Campbell and Hawke, 2005 show that reflectivity values measured at the wavelength: λ = 70 cm can be influenced by the composition of terrains buried more than 50 m deep in some cases, demonstrating the ability of this method to probe at large depth. In the case of Mars, some measurements had also been obtained using ground based radio telescopes at λ = 3.5 to 70 cm (Simpson et al., 1992; Harmon et al., 1999) or spacecraft as Mars-3 and Mars-4 spacecraft (Krupenio et al. 1977) and Viking orbiter 2 at λ = 13.1 cm (Simpson et al., 1979) but were rather limited in terms of spatial resolution and / or geographic extent. The reflectivity values obtained from these measurements have been used to estimate the dielectric constant of surface materials (Pettengill et al., 1973; Downs et al., 1973, 1975; Simpson et al., 1982). Spatial variability of the value of the dielectric constant has been interpreted in terms of variations of bulk density (Krupenio et al. 1977) and/or compositional variations (Campbell and Ulrich, 1969) of subsurface materials.

In this article, we present the method used to extract the surface echo power,

89 and the corrections required to build the global dielectric map from MARSIS
90 measurements. We show that the obtained map provides unique information on the
91 nature of the surface geological material, and more generally on Mars geology and
92 climatology.

93

2. Methods

2.1. Extraction of the surface echoes

In a first step, the surface echo power values are extracted from the data. MARSIS radargrams are composed of about a thousand frames, with each frame corresponding to a vertical sounding of the Martian surface (figure 1). Radar echoes appear when the transmitted waves meet abrupt changes in dielectric constant. The first echo in the radargram corresponds mostly to the surface echo, because lateral echoes (so called clutter) and subsurface echoes arrive later due to a longer distance between reflectors and spacecraft. Furthermore, the intensity of the surface echo is generally much higher than that of clutter or subsurface echoes. Using these characteristics, we assume that the first echo returned corresponds to surface reflection and we define a selection criteria C to localize the surface echo expressed as:

$$C(i) = \frac{|S(i)|^2}{\text{mean}(|S(i-1:i-30)|^2)} \qquad (1)$$

where S is the MARSIS signal in a given frame (512 samples) and i is the temporal index inside the frame. Equation 1 computes the contrast between a bin and the signal average over the 30-bin window preceding it.

C is maximum when $|S(i)|^2$ is maximum and $\text{mean}(|S(i-1:i-30)|^2)$, equal to the power level of the noise galactic and thermal), is minimum. This condition is only satisfied for the surface echo, i.e. the only echo that can precede the surface echo is a noise. An example of detection is given in figure 2 for orbit 2787. Once the surface

signal has been identified, the amplitude of the surface echo can easily be extracted as shown on figure 1.

We have systematically applied this process to the MARSIS data, between orbit 2300 and orbit 5200. Respectively about 0.6, 1.3 and 0.8 millions of measurements were extracted from the frequency bands centered at 3, 4 and 5 MHz. Band 1, centered at 1.8 MHz, is not used in this study because the number of measurements was too small.

2.2. Estimation of surface echo power

The surface echo power largely depends on the attenuation of the electromagnetic waves between the spacecraft and the surface, which is mainly due to range attenuation and ionospheric absorption. In the following sections, we describe the method used to correct these effects.

2.2.1. Range attenuation

Intensity of the surface echoes can be estimated by using a simplified radar equation applying Snell's law for a vertically incident electromagnetic wave on a flat surface. When we assume altitude of the satellite as R, the peak power of surface echo can be estimated as:

$$P_r = \frac{P_t G^2 \lambda^2}{4(4\pi R)^2} r_{0,1} \quad (2)$$

where P_t, G, λ and $r_{0,1}$ are the peak power of transmitted RF pulses, the antenna

gain, the wavelength and the reflectivity of the surface, respectively. Thus, the intensity of a surface echo is mainly dependent on the propagation range R, the observation wavelength $\lambda = 2\pi c/\omega$ and antenna gain G (G=1.64 for a matched dipole antenna condition).

The received power decreases with R^2 (equation 2). The Mars Express orbit is elliptical and the spacecraft altitude during MARSIS passes varies between about 250 and 1000 km. It is therefore necessary to compensate for the power losses due to altitude change, and we simply normalize the surface echo power by the squared altitude of the spacecraft.

2.2.2. Ionospheric absorption

As described by Safaeinili et al. (2003), the plasma layer (ionosphere) attenuates the MARSIS radar waves. The attenuation of electromagnetic waves per meter of ionospheric plasma is given by:

$$A = 4.61\times10^{-5}\frac{n_e(z)\nu(z)}{\omega^2+\nu(z)^2} \qquad (3)$$

where n_e is the electron density (m^{-3}) at altitude z (m), ν the electron collision frequency (rad s^{-1}) and ω is the pulsation of the radar wave (radian frequency).

For MARSIS data, we have a two-way ionospheric propagation and the total attenuation of the radar waves therefore becomes:

$$\int A dz = 2\times4.61\times10^{-5}\int\frac{n_e(z)\nu(z)}{\omega^2+\nu(z)^2}dz \qquad (4)$$

The main parameters controlling absorption (equation 4) are the electron

density and collision frequency profiles that depend on the neutral density. As these profiles are related to the ionization due to the solar EUV (extreme ultra violet) radiation, the absorption changes on Mars have a first order dependence on solar zenith angle. Safaeinili et al. (2003) have described in detail this phenomenon for different states (day/night, etc…) of the Martian ionosphere.

An accurate estimation of absorption requires knowledge of the exact state of the ionosphere and the neutral atmosphere (i.e. the density and collision profiles) for each frame. These profiles are not measured and therefore we cannot precisely calculate absorption. However, the correction of the dispersion effect (variation of wave velocity with frequency) due to the ionosphere (Safaeinili et al. 2007, Mouginot et al. 2008) provides a value of the total electron content (TEC) and, as TEC is the integral of the electron density, this value is a good proxy to estimate absorption.

Figure 3a shows that the surface echo power on MARSIS data decreases as TEC increases. In this figure, we used the entire set of signal measurements for the 4 MHz band. For a given value of TEC, the surface echo power varies over a 10dB range due to the variable reflectivity of the different Martian terrains. This trend is consistent with equation 4, which shows that electron density enhances absorption.

The signal decreases until a threshold is reached at about 30 dB below the maximum power. This threshold corresponds to the MARSIS noise level. Table 1 summarizes, for each frequency band, the values of SZA (Solar Zenith Angle) or TEC at which the signal becomes lost in the noise. We have chosen to remove the data outside the limits defined in Table 1. Furthermore, we did not use observations that show a very low signal power. In these cases, very high attenuation is probably due to the increased electron density created by precipitation and radiation during solar flares

(Espley et al. 2007).

The next step consists in evaluating the behavior of the surface echo power as a function of the TEC values. We compute the mean surface echo power for the overall data set with a bin for TEC of $2x10^{13}$ electrons per square meter. The result is presented in figure 3b. We use this curve of mean surface echo power as function of TEC to normalize the data to compensate for absorption. The normalized data plotted in figure 4 are constant on average as function of TEC.

2.3 Surface echo power

After extracting the surface echo power from the echo histories and correcting them for range dependence and ionospheric absorption, we plot the global map of the surface echo power in figure 5a. We averaged the data from multiple measurements with a bin size of 0.5 degrees. MARSIS is a nadir-looking radar and the Mars Express polar orbit does not allow us to sound the surface beyond about 87°N and 87°S. The surface echo power values for the different frequency bands are very similar and have thus been combined on this map to provide better coverage of the Martian surface. However for local or regional studies, it could also be useful in the future to compare the reflectivity measured in several frequency bands to study materials and/or structures that could change the surface reflectivity as a function of frequency (e.g., Mouginot et al. 2008).

Several parameters might affect the surface echo power: surface roughness, slope distribution and the dielectric constant of the surface materials. Most backscattering models separate the effect of the dielectric constant (material

chemistry) from those of topography (roughness, slopes) (Ulaby et al. 1986; Picardi et al. 2004). The reflectivity of the surface $r_{0,1}$ (equation 2) can be expressed by the equation:

$$r_{0,1} = \Gamma_s(\varepsilon) f_s(rms_s, \lambda) \quad (5)$$

where Γ_s is the Fresnel reflectivity terms and f_s is the backscattering term (geometric scattering). The function f_s is only dependent on the surface topography (i.e. the roughness and the slopes).

The surface roughness at MARSIS wavelength is due to slight variations of the surface heights over horizontal scale of the tens to hundred meters (figure 5c). The slope distribution effect is due to surface altitude variation on a scale of a few hundred to thousands meters. The surface echo is made from nadir return, which is a coherent specular reflection of the emitted wave at the surface interface. This nadir echo is mainly reflected on the first Fresnel zone, which has a diameter varying between 5 and 16 km (depending on the spacecraft altitude and emitted wavelength). The slope distribution inside the first Fresnel zone results in a scattering of the signal to off-nadir directions, which is related to a decrease of surface reflectivity.

As expected for a decametric radar waves, we observe in figure 5 that the roughness at kilometer-scale (Kreslavsky and Head, 2000) is highly correlated to the surface reflectivity due to slope distribution effect. The roughest terrains on Mars, such as the Olympus Mons aureole, Valles Marineris, the Argyre crater rim display very low surface echo power. Highlands Plateau, which is a heavily cratered region in the southern hemisphere, presents globally a lower reflectivity compared to the smoother northern plains (Vastistas Borealis). The smoothest terrains as the volcanic plateau in Tharsis region or Amazonis Planitia are characterized by a very high reflectivity.

Only few localized terrains that are smooth at kilometer-scale present low reflectivity, such as the linear dune regions around the north polar cap (mostly in Olympia Planitia), which are very rough at small scales and smoother at large scales (Kreslavsky and Head, 2000). An image (figure 6) provided by the High Resolution Imaging Science Experiment (HiRISE) on board Mars Reconnaissance Orbiter (MRO) illustrates this small-scale roughness, showing dunes spaced in the range of 50-100 m, which corresponds exactly to the range of MARSIS wavelength. In this particular case, the coherent part of the signal vanishes and only the incoherent part (clutter) remains, as observed on the radargrams of orbit #3674 between frames 80 and 130 (figure 6). This region is typically an area where the roughness effect on the signal is really strong compared to the effect of slope distribution.

However, only few regions are really rough at 10-100 meters scale and it seems that the main effect on surface reflectivity is due to slope distribution (kilometer-scale roughness). In addition, due to the lack of a global DEM at the required spatial resolution, we cannot model the effect of small scale (< 100 m) roughness. Thus, we have decided to neglect the effect of this roughness and to only take into account the larger-scale slope distribution. Locally, this assumption could be wrong (i.e. dune fields shown in figure 6). In such a case, we expect errors on the retrieved reflectivity values up to 3 dB (Campbell and Shepard, 2003). However, comparisons of the final dielectric map (figures 7 and 8) with the MOLA pulse width map (Neumann et al., 2003), which describes roughness at 1-20 m and SHARAD reflectivity map (unpublished data) which is sensitive to 1-15 m roughness do not show any systematic correlation at global scale. Therefore, we do not think that neglecting the < 100 roughness has any major effect for this global scale study.

2.4 Simulation of MARSIS data

In order to obtain maps showing the dielectric properties of surface materials, we have to correct for the effects of relief on the signal and then calibrate the resulting reflectivity. A method for simulating MARSIS echo histories due to local topography has been developed to help in the interpretation of the observational data. For this simulation, the surface is modeled using the facet method (Nouvel 2002; Nouvel et al. 2004), which is an extension of the Kirchhoff model. Such a model can be used because of the low surface roughness at radar wavelengths and offers a significant gain in calculation time. The synthetic faceted surface is generated from MOLA data (Smith et al. 2001).

All MARSIS orbits have been simulated and we have extracted the surface echo power in the same way as for actual MARSIS data. The dielectric constant of the surface is kept constant in the simulation. Thus, the simulation makes possible the estimation of the contribution of large-scale scattering resulting from slope distribution. We can now consider the simulation as a reference for the surface echo power in order to correct the roughness and topographic effects.

The result of all the simulations is shown in figure 5b as a global map of the expected surface echo power of the Martian surface. Note that the Olympia Planitia region is characterized by a high-simulated surface echo power compared to the real power (see figure 5a). As the facet size in the simulation is about 460 m (due to the limited MOLA resolution), the topography of the dunes is not captured by the digital elevation model. This shows the limit of the simulation that is unable to simulate the small-scale scattering resulting from surface roughness over a horizontal scale of tens of meters or less.

285 The generation of a simulated map makes it possible to normalize the surface
286 echo power extracted from the MARSIS data. Finally we estimate the Fresnel
287 reflectivity $\Gamma_s(\varepsilon)$ by dividing the MARSIS data by the simulated data (see equation 5).
288 The result of this correction is shown in figure 7.
289 The Fresnel reflection coefficient $\Gamma_s(\varepsilon)$ at normal incidence at the plane interface
290 between two media with refractive indexes n_i and n_j respectively is defined as
291 followed:

292 $$\Gamma = \frac{n_i - n_j}{n_i + n_j} \quad (6)$$

293 The relation between the dielectric constant ε and refractive index n is $n = \sqrt{\varepsilon}$. The
294 reflectivity of an interface is given by $R = |\Gamma|^2$. For the surface interface, the equation
295 6 can be reduced to:

296 $$\Gamma = \frac{1 - n_j}{1 + n_j} \quad (7)$$

297 where n_j is the refractive index of the surface materials and n_i, the refractive index of
298 the atmosphere taken as 1.
299 Using equation 7, we easily convert $\Gamma_s(\varepsilon)$ into dielectric constant.
300 As the received power is still not calibrated in an absolute way, we use the regions of
301 the North and South Polar Layered Deposits (NPLD and SPLD) as a reference. We
302 adjusted the result in figure 7 by multiplying the whole map by a constant. This
303 constant is evaluated such that the estimated water ice reflectivity values in polar
304 layered deposit is matched (Plaut et al. 2007, Grima et al. 2009). We use: $\varepsilon' = 3.1$ and
305 $\Gamma = 0.275$. We can test the validity of this method by comparing our estimates of
306 dielectric constant to the values determined in the Ascraeus Mons region by Carter et
307 al. (2009). By analyzing SHARAD radar signal propagation between the surface and

shallow interfaces, they found values of permittivity ranging from 6.2 to 17.3 in the Northern volcanic flows, with an average of 12.2, while in the southern volcanic flow, values between 7.0 and 14.0 were estimated with an average of 9.8. In the same area, the value we estimate for this area using surface power echo is of $11^{+11}_{-4}\,(n = 80)$. This result is in fair agreement with Carter et al. (2009).

3. Results and discussion

3.1 Global geographic variations

Examination of the global dielectric map (figure 7) reveals significant spatial variations over the planet. The most obvious feature is the latitude-dependent pattern in reflectivity. The equatorial region displays generally low values, the mid-latitudes generally high values, and the high latitudes generally low values again. The low-reflectivity pattern in the equatorial regions is interrupted by very high reflectivity on the Tharsis volcanic plateau, including Solis, Sinai and Daedalia plana, and the area between the Tharsis Montes and Olympus Mons. In the mid-latitude bands, the largest continuous patch of high reflectivity is on the northern side of the Elysium Mons shield. The northern high latitudes are generally lower in reflectivity than the southern high latitudes, with the exception of the area north of Alba Patera. The south residual polar cap has a very low reflectivity due to interferences within the thin layer of CO_2 ice, causing much weaker surface reflections compared to reflections from a pure water ice surface as described in details by Mouginot et al. 2009. Bands of apparent low reflectivity in the Terra Cimmeria region are probably uncorrected artifacts related to the interaction of the remnant crustal magnetics and the ionosphere (Safaeinili et al. 2007, Mouginot et al. 2008).

Two main parameters are likely to control the dielectric constant of the layer involved in the reflection process: the composition (chemistry, mineralogy, water content and physical state) and the density of the constituent materials. Because water ice presents a low dielectric constant (typically ~3.1) compared to igneous rocks (~8) at MARSIS wavelengths, the presence of a significant amount of ice in the layer

involved in the reflection process will lead to a decrease in surface reflectivity, compared to a dry, dense rock layer. However, low-density materials can also lead to such low values of the effective dielectric constant and the use of complementary datasets is crucial to build robust interpretations. We undertook systematic comparisons between the MARSIS surface dielectric map, visible albedo maps, topographic maps, the water concentration map derived from neutron spectroscopy, and the thermal inertia map derived from TES (Thermal Emission Spectrometer on Mars Global Surveyor) data.

3.2 Latitudinal variations and the onset of ground-ice

Examination of the MARSIS global map (figure 8a, b) and the corresponding longitudinally averaged profile (figure 9) reveals a strong latitudinal dependence of dielectric constant. For both hemispheres, the highest values (6 - 10) are observed at tropical latitudes. These values are in agreement with laboratory measurements on dry igneous rocks (Campbell and Ulrichs, 1969; Heggy et al., 2007) and are consistent with igneous basaltic to granitic rocks. Variations of materials density are probably responsible for the observed variability of the dielectric constant within igneous terrains.

Poleward of around 50-60° in both hemispheres, terrains show a steep decrease of dielectric constant down to values of 3 – 4. Climate related processes are likely responsible for the observed latitudinal variations (Head et al., 2003), and the comparison with other observations of the Martian surface strongly suggests that this dielectric constant decrease corresponds to the onset of water-ice occurrence within the regolith. For the current average water vapor atmospheric content, the frost point

364 at Mars surface is around 200 K. Average temperatures below the frost point are
365 reached for latitudes in excess of 30 to 45° in the Northern hemisphere and 40° in the
366 Southern hemisphere. Permanent stability of water ice is possible at depth, where the
367 sub-surface is insulated from the diurnal and seasonal temperature fluctuations. As
368 ice is not stable on the surface, we expect the ground ice to be overlaid by a layer of
369 dry regolith whose thickness depends on latitude, soil physical properties, and the
370 seasonal evolution of surface humidity (Mellon and Jakosky, 1991; Schorghofer and
371 Aharonson, 2005).

372 The MARSIS dielectric transition is not associated to a systematic change in
373 surface albedo or thermal inertia (figure 10), which implies that the surface
374 geological material does not change much upon crossing this transition. There is a
375 general agreement between the latitudinal distribution of near-surface (~top meter)
376 ground ice detected by GRS and the dielectric decrease observed by MARSIS
377 (figures 8 and 10). In the case of the southern hemisphere there is a good agreement
378 between the latitude of the ground-ice determined by MARSIS and GRS, with an
379 average latitude of 48-50°, almost constant with regard to longitude. This ground-ice
380 extent is also in good agreement with the calculated stability limit for the currently
381 observed atmospheric conditions (Mellon and Jakosky, 1991; Schorghofer and
382 Aharonson, 2005). This suggests that the icy layer is in equilibrium with the current
383 climatology.

384 In the case of the Northern hemisphere, the transition between low and high
385 reflectivity terrains is generally shifted equatorward compared to the ground-ice limit
386 detected by GRS and shows some longitudinal variations (figure 8). Most of this
387 longitudinal variability is likely related to spatial variations of the terrains' physical
388 properties and not to distribution of water ice. Particularly high dielectric values

observed at high latitudes in the north Tharsis region are likely caused by a higher density of the near-surface materials. Excluding these regions, the MARSIS ground-ice limit appears shifted equatorward by 6-7° compared to the GRS ground-ice limit. Recent evidences for the presence of ground ice at latitude as low as 43°N have been reported in Arcadia Planitia. Young craters were found to have excavated bright materials with the diagnostic spectral features of water-ice (Byrne et al., 2009). The location of these craters is consistent with the MARSIS limit of ground-ice occurrence. The bright ice deposits excavated by these young craters as well as the ground ice sampled by the Phoenix Lander both point to the presence of layers of nearly pure ice below the regolith.

Preliminary MARSIS estimates of ice fraction for the Northern latitudes (50 – 100 % by volume, see section 3.3) would also imply the presence of water ice in excess of the regolith porosity. In the Southern hemisphere, estimated values do not allow us to firmly constrain the origin of ground ice. Such a mode of occurrence is inconsistent with pore-filling ice emplaced by direct condensation from atmospheric water vapor. It requires the deposition of an ice-rich material on the surface, such as frost or snow, then buried under a layer of dry regolith formed either by sublimation of dusty ice or by wind transport. Morphologic evidences support this interpretation for both Northern and Southern ground-ice (Head et al., 2003). Repeated freeze thaw (due to long-term variations in obliquity) of an initially ice-saturated regolith can also result in the migration of thin films of adsorbed water along mineral grain surfaces in response to the presence of a temperature gradient. On Earth, this process can result in the formation of massive ice deposits/lenses (Washburn 1980; Williams and Smith 1989), which could also explain the Phoenix and GRS observations. However, this mechanism is unlikely to explain ice concentrations of 50-100% to depth >60 m into

414 the subsurface. Beyond the in situ enrichment of ice by repeated freeze/thaw (or the
415 deposition of massive mantles of ice) in response to obliquity variations, there is also
416 the potential survival of water discharged by the outflow channels (Carr 1990) – or
417 the survival of frozen relic of an early ocean (Clifford and Parker, 2001).

418

419 **3.3 Estimation of the volume of water-ice seen by MARSIS**

420

421 The aim of this paragraph is to propose a rough first order estimate of the
422 water-ice content of the ground based on reflectivity values measured by MARSIS in
423 a simple and ideal case. The accurate inversion of reflectivity values in terms of
424 ground ice content is indeed a challenging task that requires a complete physical
425 modeling of the radar waves reflection process and the knowledge of various
426 properties of the ground. If some of these properties remain unconstrained (layering,
427 density…), it is likely that different models of subsurface composition and structure
428 can lead to similar values of reflectivity, i.e. the inversion process does not lead to a
429 unique solution. Our future work on the retrieval of subsurface composition and
430 texture from MARSIS absolute reflectivity values, based on physical modeling, will
431 be focused on these issues but is beyond the scope of this first study. Here, we
432 calculate the order of magnitude of the amount of water ice required in the subsurface
433 to account for the values of reflectivity measured by MARSIS assuming a
434 homogeneous composition at the scale of a MARSIS resolution cell and fixed
435 parameters for the texture of the ground. By doing that, we aim to provide to the
436 reader an idea of the quantity of ice that can be probed by our method and set a
437 starting point for future studies that will refine the rough value estimated here. In the
438 framework of the simple investigated hypothesis, two values have to be estimated to

calculate the quantity of water ice: the thickness of the layer probed by the reflection of the electromagnetic waves on the surface and the ice/rock ratio in this homogeneous layer.

3.3.1 Thickness of the probed layer

The reflectivity coefficient we determine is related to the permittivity of the surface materials. If one supposes that the subsurface is an infinite homogenous half-space, MARSIS is directly probing the specular reflection of the radar wave. The depth involved in the reflection process is thus given by the skin effect. The loss is given by:

$$\alpha = 0.091 f \sqrt{\varepsilon} \tan(\delta)$$

Where f is the frequency (in MHz) and $\tan(\delta)$ the loss tangent.

From the value of α one might calculate the skin depth by using:

$$d = \frac{10 \log_{10} e}{\alpha}$$

Loss tangent for Mars surface rocky materials are expected to vary between 0.004 and 0.03 (Picardi et al., 2004) at 5 MHz and were measured to be within the 0.01-0.03 range (at 20 MHz) for lava flows west of Ascraeus Mons (Carter et al., 2009). Using 0.004 and 0.03 as likely extreme values for the loss tangent, we find the corresponding values for the skin depth to be 780 and 100 m respectively.

The MARSIS radar signal has a temporal resolution of $\Delta t = 1$ µs that is equivalent to a propagation length in the media of $2L = c\Delta t / \sqrt{\varepsilon}$ Because this distance is smaller

than the skin thickness *d*, the probed depth in the surface echo is controlled by the temporal resolution. For $\varepsilon = 6$ and 3, this resolution is of 60 to 80 m respectively. It is important to note that this probed thickness is considerably larger than for other usual remote-sensing methods like visible-NIR imaging and spectroscopy (a few μm) or neutrons and gamma-ray spectroscopy (a few tens of cm).

3.3.2 Ice/rock ratio

In the simple case of a two components mixture examined here, mixing ratios between rock and ice can be roughly estimated using the Maxwell-Garnet rules (Maxwel Garnett, 1904). Maxwell-Garnett rules assume an asymmetric binary mixture with a matrix or environment of dielectric constant: ε_e and spherical inclusions of dielectric constant: ε_i. The medium is assumed to be isotropic. Let f be the volumetric fraction of inclusions in the mixture. The Maxwell-Garnet mixing formula allows us to calculate the effective dielectric constant, ε_{eff}, of the binary mixture:

$$\varepsilon_{eff} = \varepsilon_e + 3f\varepsilon_e \frac{\varepsilon_i - \varepsilon_e}{\varepsilon_i + 2\varepsilon_e - f(\varepsilon_i - \varepsilon_e)} \quad (10)$$

The inversion of dielectric constant value measured by MARSIS in terms of ice / rock ratio requires the knowledge of the dielectric constants of the pure end-members. If the value of ε' = 3.1 for pure water ice at MARSIS wavelength is commonly accepted (Petrenko, 1999) and is not likely to be subject to strong spatial or temporal variations, the choice of a value for the rocky component of the mixture is more problematic. Usually the dielectric constants for volcanic rocky materials are

484 comprised between 6 and 11 (Campbell and Ulrichs, 1969). The mean value found in
485 tropical regions by MARSIS is 6.5. Thus, we assume that the dielectric constant of the
486 dry rock chosen for our calculations are the same as the one measured by MARSIS in
487 equatorial regions. The chosen value is relatively low and even if the nature of the soil
488 changes in certain regions, we can give a lower estimate of the ice / rock mixing ratio.
489 We obtain values of the ice / rock volume mixing ratio of the order of 50 % in the
490 Southern and between 50 and 100 % in the Northern. Although the variability is high,
491 it appears that the average amount of ice present in the subsurface is higher in the
492 Northern hemisphere that in the Southern hemisphere. Furthermore, other
493 observations point to systematic differences between the two hemispheres (see section
494 3.3).

495 The total amount of water stored in the two Martian polar layered terrains
496 (Plaut et al., 2007, Smith et al., 2001) is estimated to be 2.8 10^6 km^3. The atmosphere
497 contains the equivalent of ~3 km^3 of condensed water (Plaut et al., 2001). The total
498 amount of water contained in the subsurface is certainly the main uncertainty in the
499 current inventory of water on Mars. While neutron spectroscopy permitted an
500 estimation of the amount and extent of ice in the top meter of the regolith, low
501 frequency radar techniques now offer the unique opportunity to probe the regolith and
502 quantify the amount of ice at decameters to kilometers scale. In the framework of the
503 ideal hypothesis of a homogeneous subsurface considered in this paragraph, we can
504 estimate the total amount of ground water ice necessary to explain the low values of
505 reflectivity measured by MARSIS. Considering the measured extent of both Northern
506 and Southern ground-ice, the average ice / rock ratio obtained from inversion of
507 MARSIS dielectric measurements and a probed thickness of 60-80 meters, we
508 estimate the potential lower limit of the total volume of ice currently stored at high

latitude in the ground to be ~10^6 km^3, of the order of magnitude of the volume of one of the polar caps. As already mentioned at the beginning of this paragraph, future studies dedicated to the physical modeling of the radar reflection process should now be undertaken to examine the influence of the heterogeneity of the subsurface on the inversion of dielectric values in terms of amount of water ice in the subsurface. The case of meters-thick lenses of pure water ice close to the surface should be investigated in priority as this ground structure has been mentioned to interpret recent datasets, especially in-situ observations by the Phoenix Lander (Smith et al., 2009).

3.4 Tropical and equatorial minima

Examination of the MARSIS surface dielectric map in the equatorial to tropical regions reveals the occurrence of a nearly continuous low reflectivity belt between -30° and +30° latitude. Extremely low values are reached in the Medussae Fossae area ($\varepsilon \approx 3$) (figure 8 and 10). Other minima are encountered in the areas of Meridiani Planum ($\varepsilon \approx 4$) and from Isidis basin to the highlands south of Elysium Planitia ($\varepsilon = 3.5$). The low values of dielectric constants can have various origins: different composition of rocks, low density of surface material, presence of water ice buried beneath a desiccated regolith… Radar measurements alone do not allow discriminating between these different possibilities. When compared to other datasets, it appears that, as in the polar regions, the best match for the MARSIS reflectivity equatorial pattern is obtained from comparison with the GRS WEH map. Indeed, the low reflectivity regions roughly correspond to regions that were shown to be enriched in hydrogen by the GRS instrument suite, with WEH values up to 12%. The interpretation of high hydrogen enrichments detected by GRS in the top first meter of the regolith is still debated. Different explanations have been proposed, like a high abundance of nominally hydrated minerals (Fialips et al., 2005), an interaction of the regolith with atmospheric water vapor (Feldman et al., 2005), or the presence of transient ground ice (Jakosky et al., 2005).

The spatial agreement between the low-reflectivity values on the MARSIS map and the H-enriched areas on the GRS map strongly points toward a water-related explanation. In particular, the Medusae Fossae formation terrains, when sounded by MARSIS (Watters et al., 2007), were found to have a bulk real dielectric constant $\varepsilon = 2.9 \pm 0.4$, in agreement with our near-surface estimate. The authors proposed two

hypotheses to explain these low values: low-density volcanic deposits or the presence of ice, deposited during a high-obliquity/high-humidity climatic excursion that is currently sublimating at some depth and hydrating the overlying regolith. Spatial correlation between MARSIS and GRS measurements supports this last hypothesis. Unfortunately, the new MARSIS results do not generally allow arguing in favor or one or another of the hypotheses proposed to explain high WEH values measured by GRS. Indeed, the presence of low density / highly hydrated sedimentary materials, such as the ones observed in-situ by the Opportunity rover in Meridiani Planum (Squyres et al., 2004) could explain the observed low radar reflectivity because of their low dielectric constant (Campbell and Ulrichs, 1969) as well as the presence of ground ice as already discussed for high latitudes regions.

If the MARSIS radar map does not allow us to choose unambiguously between the pre-cited mechanisms, its main implication is that anomalous surface hydrogen enrichments detected by GRS correspond to anomalies of dielectric constant, possibly related to the presence of H_2O in an unconstrained state, extending down to at least a few decameters below the surface. This is a new and important constraint on the nature and origin of the equatorial anomalies that should be taken into account in future interpretations of these regions.

Conclusion

A global 3-5 MHz dielectric map of the Martian surface is built from two years of measurements by the MARSIS instrument. Using MOLA topographic data, we corrected the effect of kilometer-scale roughness and slopes to retrieve the spatial variations of the dielectric constant of near-surface materials. Many parameters are susceptible to influence the dielectric constant of the top decameters below the surface that are probed by the radar wave reflection process. With the use of complementary datasets, we were able to interpret the geographic variations of radar reflectivity in term of surface geological material. From the comparison of the MARSIS map with the hydrogen abundance map derived from GRS measurements, we show that low dielectric values at latitudes poleward of 50-60° are likely to be due to high amount of water ice in the ground.

The thickness probed by the MARSIS surface reflectivity is of the order of a few decameters, resulting in a significant increase of the total quantity of ground ice compared to GRS observations, only representative of the first meter below the surface. Assuming a homogenous composition of the ground at the scale of a MARSIS resolution cell as a simple first-order hypothesis, measured values of dielectric constant lead to a minimum estimate of ice stored in the Martian sub-surface to be of the order ~10^6 km^3, equivalent to a polar cap. Future studies focused on the physical modeling of the reflection process over more realistic models of the subsurface structure and texture will be necessary to refine this rough estimation.

At least in the Northern hemisphere the amount of ice appears to be in excess of porosity. Refined analysis of the frequency dependence of the surface reflectivity, together with laboratory measurements of the dispersion relation of ice-rock mixture

might help in confirming this observation that would have strong implication for the mechanism of ground ice emplacement.

Puzzling anomalies in hydrogen at equatorial latitudes first revealed by the GRS instrument correspond to low reflectivity areas on the MARSIS map. If low reflectivity alone does not permit to discuss further the origin of the hydrogen anomalies, presence of highly hydrated minerals or shallow buried ice, it tells us that the anomalies identified by GRS in the near subsurface actually extend in depth to the first decameters below the surface.

Acknowledgments

This article is dedicated to the memory of Ali Safaeinili (1964-2009) and his immeasurable contribution to radar sounder development and scientific exploitation.

The authors would like to thank the reviewers (Clifford S.M. and Campbell B.A.) for their comments that help improve the manuscript.

We acknowledge the support of the space agencies of Italy (ASI) and the United States (NASA), for the development and science operations of MARSIS. Operations of the Mars Express spacecraft by the European Space Agency (ESA) are gratefully acknowledged. The French space agency (CNES) supports these studies in Laboratoire de Planétologie de Grenoble.

609 # References

610 Aharonson, O., Zuber, M. T. and Rothman, D. H., 2001. Statistics of Mars'
611 topography from the Mars Orbiter Laser Altimeter: Slopes, correlations, and physical
612 models*, J. Geophys. Res., 106*, 23723-23736, doi: 10.1029/2000JE001403

613 Boynton, W. V, and 24 colleagues, 2002. Distribution of Hydrogen in the Near
614 Surface of Mars: Evidence for Subsurface Ice Deposits, *Science, 297*, 81-85

615 Boynton, W. V., and 27 colleagues, 2007. Concentration of H, Si, Cl, K, Fe, and Th in
616 the low- and mid-latitude regions of Mars. Journal of Geophysical Research-Planets.
617 112, 15.

618 Byrne, S., and 17 colleagues, 2009. Distribution of Mid-latitude Ground Ice on Mars
619 from New Impact Craters, *Science*, 325, 1674-1680.

620 Campbell, M. J., Ulrichs, J., 1969. Electrical properties of rocks and their significance
621 for lunar radar observations*, J. Geophys. Res., 74*, 5867-5881.

622 Campbell, B. A., Shepard, M. K., 2003. Coherent and incoherent components in near-
623 nadir radar scattering: Applications to radar sounding of Mars, *J. Geophys. Res.*,
624 Volume 108, Issue E12, pp. 6-1.

625 Campbell, B. A., Hawke, B R., 2005. Radar mapping of lunar cryptomaria east of
626 Orientale basin, *J. Geophys. Res.*, 110, doi :10.1029/2005JE002425.

627 Carr, M. H., 1990. D/H on Mars - Effects of floods, volcanism, impacts, and polar
628 processes, *Icarus* (ISSN 0019-1035), vol. 87, Sept. 1990, p. 210-227.

629 Carter, L. M., et al., 2009. Dielectric properties of lava flows west of Ascraeus Mons.
630 *Geophysical Research Letters*. 36**,** doi:10.1029/2009GL041234.

631 Clifford, S. M., 1993. A model for the hydrologic and climatic behavior of water on
632 Mars. *J. Geoph. Res.*, 98, 10973.

633 Clifford, S. M.; Parker, T. J., 2001. The Evolution of the Martian Hydrosphere:
634 Implications for the Fate of a Primordial Ocean and the Current State of the Northern
635 Plains, *Icarus*, Volume 154, Issue 1, pp. 40-79.

636 Connerney, J. E. P., Acuña, M., Wasilewski, P. J., Kletetschka, G., Ness, N. F.,
637 Rème, H., Lin, R. P., Mitchell, D. L., 2001. The Global Magnetic Field of Mars and
638 Implications for Crustal Evolution, *Geoph. Res. Let.*, *28*, 4015-4018, doi:
639 10.1029/2001GL013619.

640 Downs, G. S., Goldstein, R. M., Green, R. R., Morris G. A. and Reichley, P. E. 1973.
641 Martian topography and surface properties as seen by radar: The 1971 opposition.
642 *Icarus*, 18, 8-21.

643 Downs, G. S., Reichley, P. E. and Green, R. R. 1975. Radar measurements of Martian
644 topography and surface properties : The 1971 and 1973 oppositions. *Icarus*, 26, 273-
645 312.

646 Duru, F., Gurnett, D., Averkamp, T., Kirchner, D., Huff, R., Persoon, A., Plaut, J.,
647 Picardi, G., 2006. Magnetically controlled structures in the ionosphere of Mars *J.*
648 *Geophys. Res., 111*, 12204-+, doi: 10.1029/2006JA011975.

649 Espley, J., R., Farrell, W., Brain, V, Morgan, V, Cantor, B., Plaut, V, Acuña, M.,
650 Picardi, G., 2007. Absorption of MARSIS radar signals: Solar energetic particles and
651 the daytime ionosphere, *Geoph. Res. Let., 34*, 9101-+, doi: 10.1029/2006GL028829.

652 Evans, J. V. 1962. Radio echoes studies of the Moon. In *Physics and Astronomy of the*
653 *Moon*, ed. Z. Kopal (Nea York : Academic Press), pp 429-479

654 Evans, J. V. and Pettengill, G. H. 1963. The scattering behavior of the Moon at
655 wavelengths of 3.6, 68, and 784 centimeters. *J. Geophys. Res*. 68, 423-477.

656 Feldman, W. C., and 12 colleagues, 2002. Global Distribution of Neutrons from Mars:
657 Results from Mars Odyssey, *Science, 297*, 75-78

658 Feldman, W. C. and 14 colleagues, 2004. Global distribution of near-surface
659 hydrogen on Mars, *J. Geophys. Res., 109*, 9006-+, doi: 10.1029/2003JE002160.

660 Feldman, W. C., Prettyman, T. H., Maurice, S., Nelli, S., Elphic, R., Funsten, H. O.,
661 Gasnault, O., Lawrence, D. J., Murphy, J. R., Tokar, R. L., and Vaniman, D. T., 2005.
662 Topographic control of hydrogen deposits at low latitudes to midlatitudes of
663 Mars, J. Geophys. Res., 110, doi : 10.1029/2005JE002452.

664 Fialips, C. I., Carey, J. W., Vaniman, D. T., Bish, D. L., Feldman, W. C., and Mellon, M.
665 T., 2005. Hydration state of zeolites, clays, and hydrated salts under present-day
666 martian surface conditions: Can hydrous minerals account for Mars Odyssey
667 observations of near-equatorial water-equivalent hydrogen?, Icarus, 178, 74-83.

668 Fung, A. K., Li, Z., Chen, K. S., 1992. Backscattering from a randomly rough
669 dielectric surface, *IEEE Transactions on Geoscience and Remote Sensing, 30*, 356-
670 369

671 Grima, C., Kofman, W., Mouginot, J., Phillips, R., J., Hérique, A., Biccari, D., Seu,
672 R., Cutigni, M., 2009. North polar deposits of Mars: Extreme purity of the water ice,
673 *Geoph. Res. Let., 36*, 3203-+

674 Gurnett, D., and 10 colleagues, 2005. Radar Soundings of the Ionosphere of Mars
675 *Science, 310*, 1929-1933.

676 Head, J. W., Mustard, J. F., Kreslavsky, M. A., Milliken, R. E., Marchant, D. R.,
677 2003. Recent ice ages on Mars. *Nature*. 426, 797-802.

678 Heggy, E., Paillou, P., Costard, F., Mangold, N., Ruffie, G., Demontoux, F.,
679 Grandjean, G., Malézieux, J. M., 2003. Local geoelectrical models of the Martian
680 subsurface for shallow groundwater detection using sounding radars *J. Geophys. Res.*,
681 *108*, 11-+, doi: 10.1029/2002JE001871.

682 Heggy, E., Clifford, S. M., Younsi, A., Miane, J. L., Carley, R., Morris, R. V., 2007.
683 On the Dielectric Properties of Dust and Ice-Dust Mixtures: Experimental
684 Characterization of the Martian Polar-layered Deposits Analog Materials. *Lunar and*
685 *Planetary Institute Conference Abstracts*, Vol. 38, 2007, pp. 1756.

686 Jakosky, B. M., Mellon, M. T., Varnes, E. S., Feldman, W. C., Boynton, W. V.,
687 Haberle, R. M., 2005. Mars low-latitude neutron distribution: Possible remnant near-
688 surface water ice and a mechanism for its recent emplacement, *Icarus*, 175, 58-67.
689

690 Kreslavsky, M., A., Head, J. W., 2000. Kilometer-scale roughness of Mars: Results
691 from MOLA data analysis, *J. Geophys. Res.,* 105, 26695-26712,
692 doi:10.1029/2000JE001259.

693 Krupenio, N. N., 1977. Map-plot of the dielectric constant and density of Martian
694 surface soil, *Kosmicheskie Issledovaniia*, 15, 470-474.

695 Leblanc, F., and 14 colleagues, 2008. Observations of aurorae by SPICAM ultraviolet
696 spectrograph on board Mars Express: Simultaneous ASPERA-3 and MARSIS
697 measurements, *J. Geophys. Res., 113*, 8311-+, doi: 10.1029/2008JA013033.

698 Mangold, N., 2005. High latitude patterned grounds on Mars: Classification,

699 distribution and climatic control. *Icarus*. 174, 336-359.

700 Maxwell Garnett, J. C., 1904. Colours in metal glasses and metal films. *Transaction*
701 *of the Royal Society of London* **CCIII**, 481-502.

702 Mellon, M., Jakosky, B. M., 1993. Geographic variations in the thermal and diffusive
703 stability of ground ice on Mars. *Journal of Geophysical Research*. 98, 3345-3364.

704 Mellon, M. T., Feldman, W. C., Prettyman, T. H., 2004. The presence and stability of
705 ground ice in the southern hemisphere of Mars. *Icarus*. 169, 324-340.

706 Mellon, M. T., Arvidson, R. E., Marlow, J. J., Phillips, R. J., Asphaug, E., 2008.
707 Periglacial landforms at the Phoenix landing site and the northern plains of Mars.
708 *Journal of Geophysical Research-Planets*. 113.

709 Mitrofanov, I., and 11 colleagues, 2002. Maps of Subsurface Hydrogen from the High
710 Energy Neutron Detector, Mars Odyssey, *Science, 297*, 78-81.

711 Mouginot, J., Kofman, W., Safaeinili, A., Herique, A., 2008. Correction of the
712 ionospheric distortion on the MARSIS surface sounding echoes*, Plan. and Space Sci.,*
713 *56*, 917-926

714 Mouginot, J., Kofman, W., Safaeinili, A., Grima, C., Herique, A., Plaut, J.~J. 2009.
715 MARSIS surface reflectivity of the south residual cap of Mars, *Icarus* 201, 454-459
716 Niles, P. B., Michalski, J., 2009. Meridiani Planum sediments on Mars formed
717 through weathering in massive ice deposits. *Nature Geoscience*. 2, 215-220.

718 Neumann, G. A.; Abshire, J. B.; Aharonson, O.; Garvin, J. B.; Sun, X.; Zuber, M. T.,
719 2003. Mars Orbiter Laser Altimeter pulse width measurements and footprint-scale
720 roughness, *Geophysical Research Letters*, Volume 30, Issue 11, pp. 15-1.

721 Nouvel, J. F., 2002. Sondage du sous-sol martien par un radar basse-fréquence depuis
722 un satellite en orbite basse: analyses physiques et préparation des données, PhD
723 Thesis, *Université Joseph Fourier, Grenoble.*

724 Nouvel, J., F., Herique, A., Kofman, W., Safaeinili, A., 2004. Radar signal
725 simulation: Surface modeling with the Facet Method, *Radio Sci., 39*, RS1013

726 Petrenko, V. F., Whitworth, R. W., 1999. *Physics of Ice*. Oxford Univ. Press, New
727 York.

728 Pettengill, G. H., Shapiro, I. I., and Rogers, A. E. E. 1973. Topography and radar
729 scattering properties of Mars. Icarus, 18, 22-28.

730 Picardi, G., and 12 colleagues, 2004. Performance and surface scattering models for
731 the Mars Advanced Radar for Subsurface and Ionosphere Sounding (MARSIS).
732 Planetary and Space Science. 52, 149-156.

733 Picardi, G., and 33 colleagues, 2005. Radar Soundings of the Subsurface of Mars,
734 *Science, 310*, 1925-1928.

735 Plaut, J., J., and 23 colleagues, 2007. Subsurface Radar Sounding of the South Polar
736 Layered Deposits of Mars, *Science, 316*, 92-95.

737 Safaeinili, A., Kofman, W., Nouvel, J. F., Herique, A., Jordan, R., 2003.
738 Impact of Mars ionosphere on orbital radar sounder operation and data processing,
739 *Plan. and Space Sci., 51*, 505-515.

740 Safaeinili, A., Kofman, W., Mouginot, J., Gim, V, Herique, A., Ivanov, A., Plaut, J.,
741 Picardi, G., 2007. Estimation of the total electron content of the Martian ionosphere
742 using radar sounder surface echoes, *Geoph. Res. Let., 34*, 23204-+,

743 doi:10.1029/2007GL032154.

744 Schorghofer, N., Aharonson, O., 2005. Stability and exchange of subsurface ice on
745 Mars. Journal of Geophysical Research-Planets. 110, 16.

746 Seu, R., and 11 colleagues, 2007. SHARAD sounding radar on the Mars
747 Reconnaissance Orbiter, J. Geophys. Res., 112, doi :10.1029/2006JE002745.

748 Sihvola, A., 1999. *Electromagnetic mixing formulas and applications*. IEEE.

749 Simpson, R. A., Tyler, G. L., Brenkle, J. P. and Sue, M. 1979. Viking bistatic radar
750 observations of the Hellas Basin on Mars: Preliminary results, *Science*, 203, 153-173.

751 Simpson, R. A., Tyler, G. L. Harmon, J. K. and Peterfreund, A. R. 1982. Radar
752 measurement of small-scale surface texture : Syrtis Major, *Icarus*, 49, 258-283.

753 Simpson, R. A, Harmon, J. K, Zisk, S. H, Thompson, T.~W. and Muhleman, D. O.
754 1992. Radar determination of Mars surface properties in *Mars*, The university of
755 Arizona Press, p. 652-685.

756 Smith, D. E., and 23 colleagues, 2001. Mars Orbiter Laser Altimeter: Experiment
757 summary after the first year of global mapping of Mars*, J. Geophys. Res., 106*, 23689-
758 23722, doi:10.1029/2000JE001364.

759 Smith, M. D., 2004. Interannual variability in TES atmospheric observations of Mars
760 during 1999-2003. Icarus. 167, 148-165.

761 Smith, P. H., and 35 colleagues, 2009. H_2O at the Phoenix landing site. Science, 325,
762 58-61.

763 Squyres, S. W., Clifford, S. M., Kuzmin, R. O., Zimbelman, J. R., Costard, F. M.,
764 1992. Ice in the Martian Regolith. In: H. H. Kieffer, (Ed.), Mars. The University of

765 Arizona Press.

766 Squyres, S. W., and 18 colleagues, 2004. In Situ Evidence for an Ancient Aqueous
767 Environment at Meridiani Planum, Mars. Science. 306, 1709-1714.

768 Ulaby, F., Moore, T. R., Fung, A., 1986. Microwave Remote Sensing, Artech House
769 Publishers.

770 Washburn, A. L., 1980. Permafrost features as evidence of climatic change, *Earth*
771 *Science Reviews,* Volume 15, Issue 4, p. 327-402.

772 Watters, T. R., and 12 colleagues, 2007. Radar Sounding of the Medusae Fossae
773 Formation Mars: Equatorial Ice or Dry, Low-Density Deposits?, *Science,* 2007*, 318*,
774 1025.

775 Williams P. J., Smith M. W., 1989. The Frozen Earth: Fundamentals of Geocryology,
776 Cambridge University Press, , Cambridge (1989). ISBN 0 521 365334 1.

777

778
779

780

781

782

Figure Captions

Figure 1: Top: a typical MARSIS pulse measured over the South Polar Layered Deposits (orbit #2682, pulse 718) in dB. The surface echo is recorded at about t = 130 µs after the opening of the receiver's window. Another strong echo, attributed to the reflection on the bedrock below this ice, is received at t = 170 µs. Bottom: the criteria C as defined in equation 1 calculated for the same MARSIS pulse. The position of the surface echo is indisputably highlighted by the high value of *C*,

Figure 2. Top to bottom: the radargram of orbit #2787, the position of the surface echo detected by our algorithm, the power reflected by the surface in dB.

Figure 3 (a) Left: raw reflectivity as function of the Solar Zenith Angle (SZA). (b) Right: mean reflectivity as function of the Total Electron Content. Both graphics have been plotted using the entire set of data at 4 MHz.

Figure 4. Reflectivity corrected for absorption as function of the total electron content. The graph has been plotted using the entire set of data at 4 MHz.

Figure 5. A: Reflectivity map at 3-5 MHz of the Martian surface as seen by MARSIS. Red corresponds to high reflectivity and blue to low reflectivity. Grey regions correspond to a lack of data. The map is in cylindrical projection. The spatial resolution is 0.5 bin per degree.

B: Reflectivity map based on simulated radargrams. Grey regions correspond to a lack of data. The map is a cylindrical projection. The resolution is 0.5 bin per degree.

C: Roughness map from Kreslavsky and Head (2000)

Figure 6. The image on the left has been provided by HIRISE on board MRO (PSP_001736_2605, credit: NASA/JPL/University of Arizona). This image with 25 cm resolution per pixel shows in detail the dunes in Olympia Undae. The radargram on top corresponds to a part of orbit #3674 of MARSIS/MEX over this region. The bottom image is the MOLA topography corresponding to the MARSIS track.

Figure 7. Reflectivity map corrected for roughness effect. As described in the text, the reflectivity has been calibrated using a reference making it possible to provide the corresponding dielectric constant. The map is a cylindrical projection. The spatial resolution is one bin per degree. Grey background corresponds either to a lack of data or a removal of data corrupted by artefacts (effects of magnetic field, high surface roughness).

Figure 8: (A) MARSIS dielectric map. Same as figure 7.

(B) Global interpolation of the dielectric map (A) using 8-order spherical harmonics adjustment.

(C) Global map of hydrogen concentration in the top meter of the regolith obtained by the neutrons spectrometer of the GRS / Mars Odyssey instruments suite (data from Feldman et al., 2004). Concentration is expressed as Water Equivalent Hydrogen abundance in weight percent.

All maps are gridded in Robinson projection.

Figure 9: Longitudinal averages of MARSIS surface real dielectric constant and GRS neutrons spectrometer WEH concentration. Red crosses correspond to the dielectric constant values measured by MARSIS and plotted on figure 8.A whereas the red

828 curve corresponds to the interpolated MARSIS map (figure 8.B). WEH values are
829 calculated from the map plotted in figure 8.C.

830 **Figure 10**: A: Visible color map (Viking), B: Thermal inertia map (TES), C:
831 MARSIS reflectivity map. The comparison between these maps shows that the limits
832 displayed on the MARSIS reflectivity map do not correspond to systematic changes
833 of albedo and thermal inertia, indicating that the surface material remains unchanged
834 while subsurface material is different.

835 # Tables

Central Frequency	3 MHz	4 MHz	5 MHz
Total electron Content ($10^{15}m^{-2}$)	3	7.5	7.5
Solar Zenith Angle	85°	70°	60°

836

837 **Table 1**. Summary of the limits used to select the data. Measurements are kept when
838 the total electron content is below the limit indicated by the first line and when the
839 solar zenith angles are above the limit indicated by the second line.

840

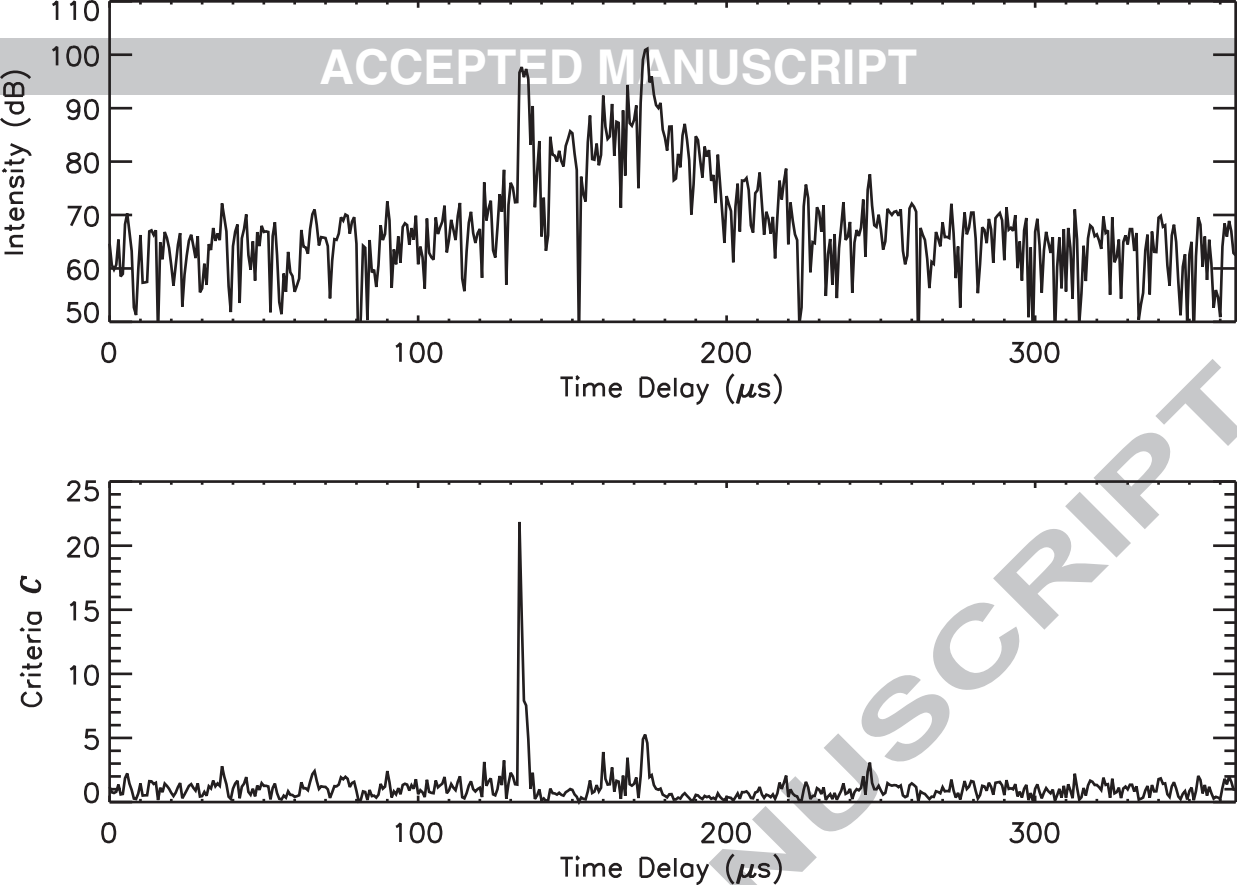

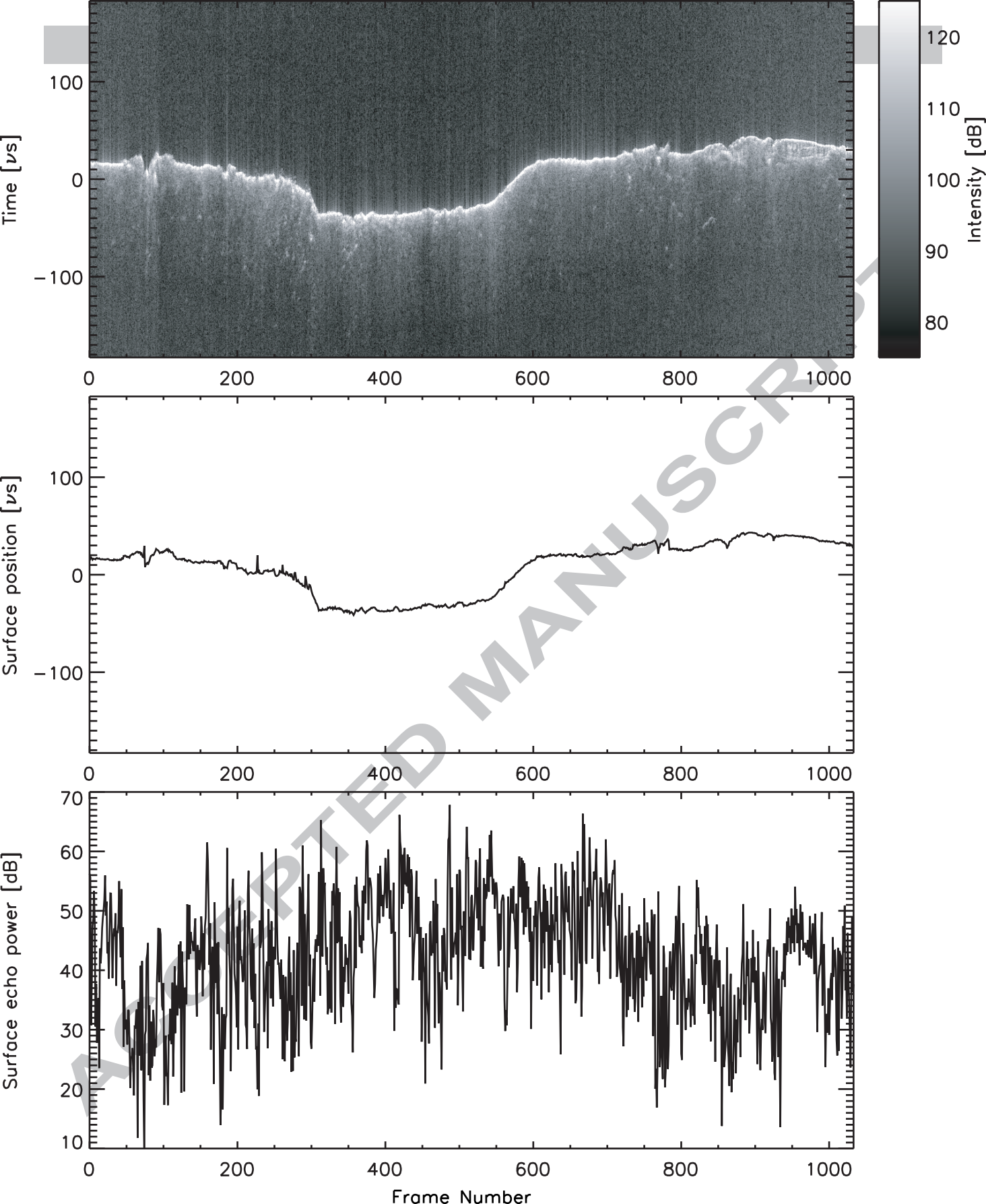

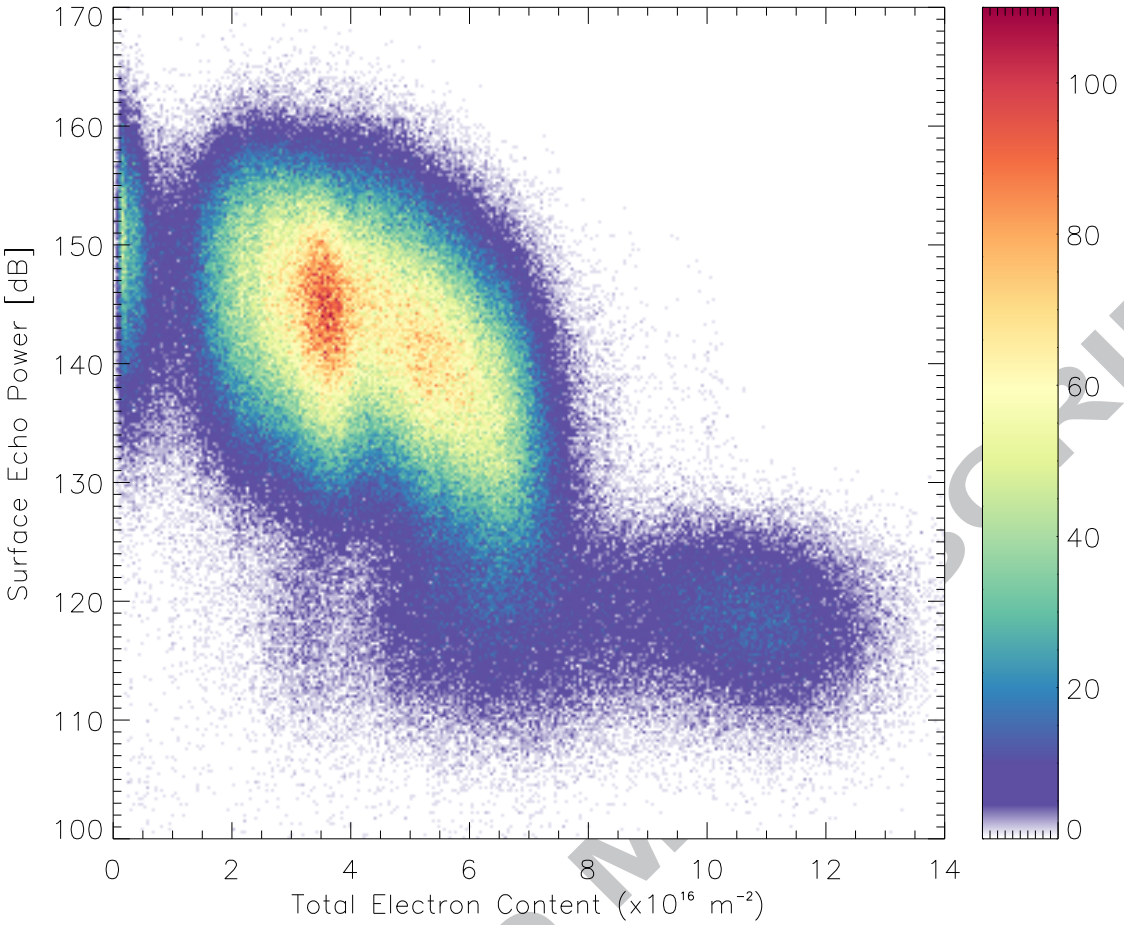

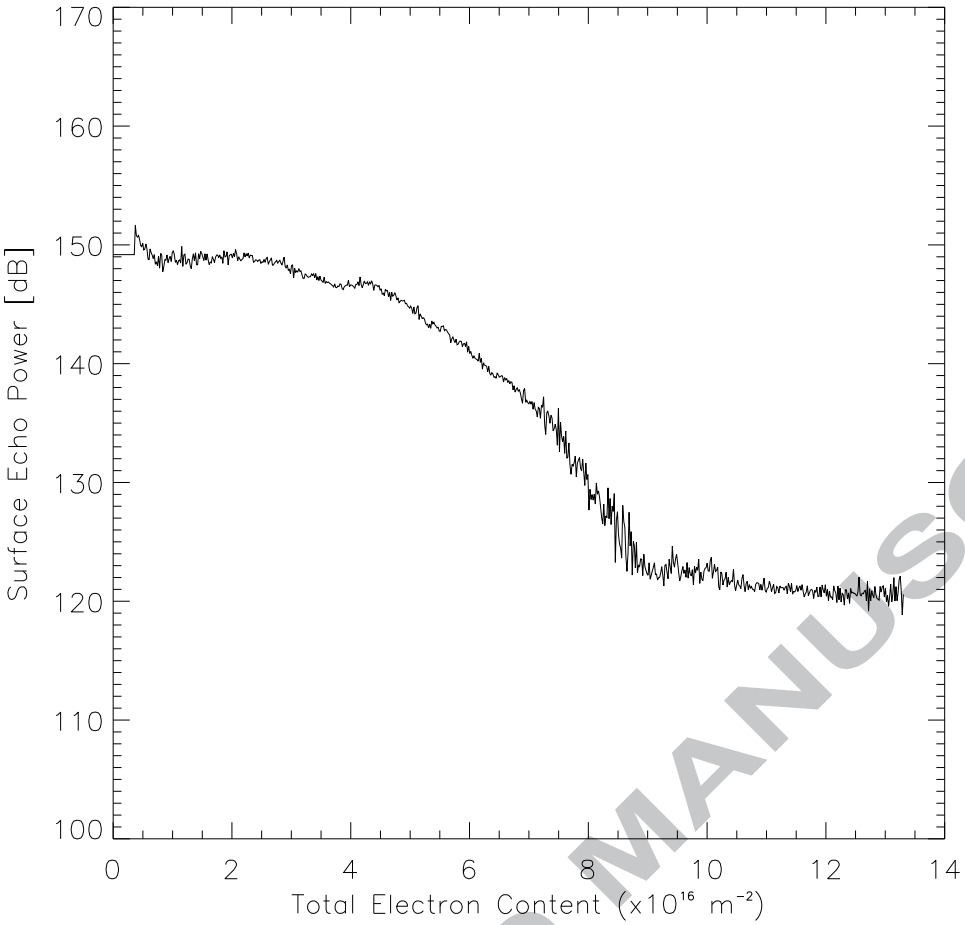

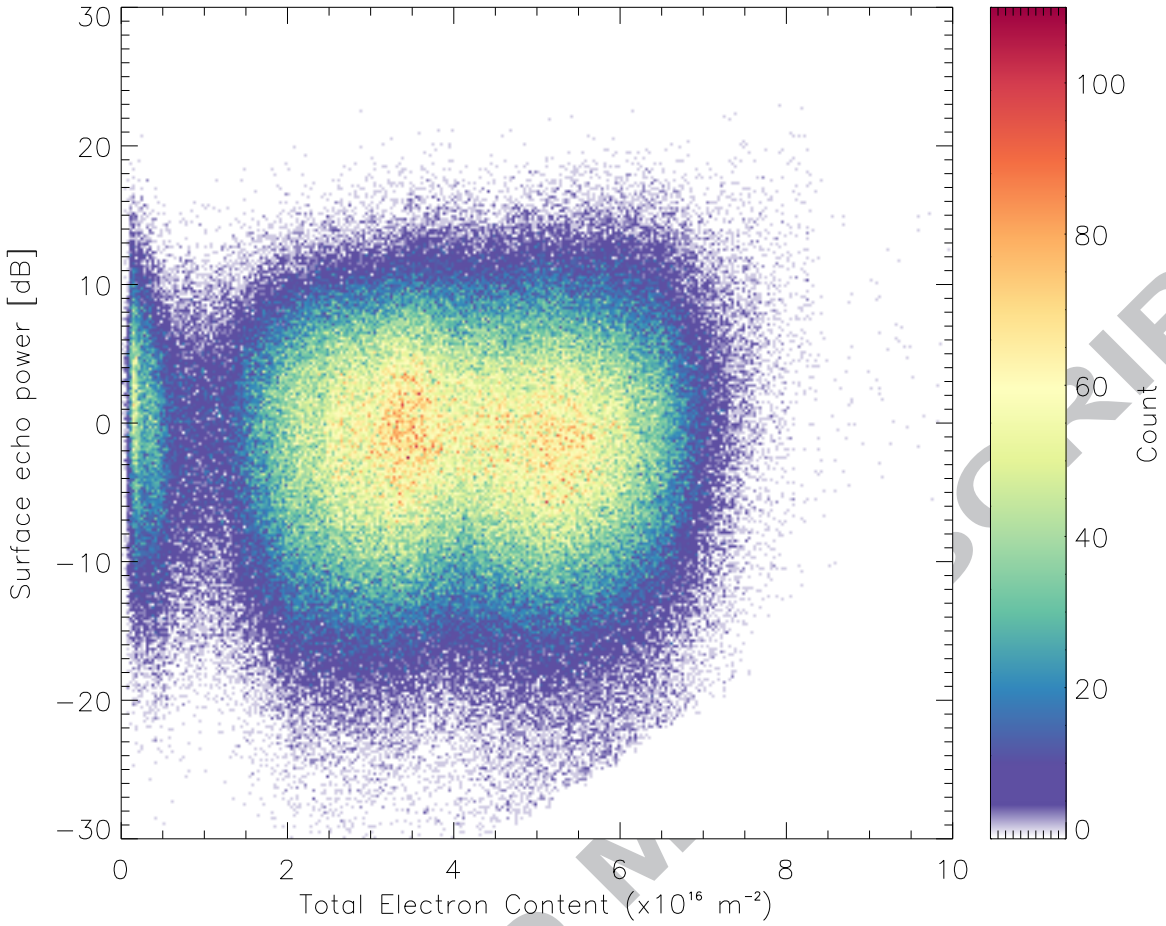

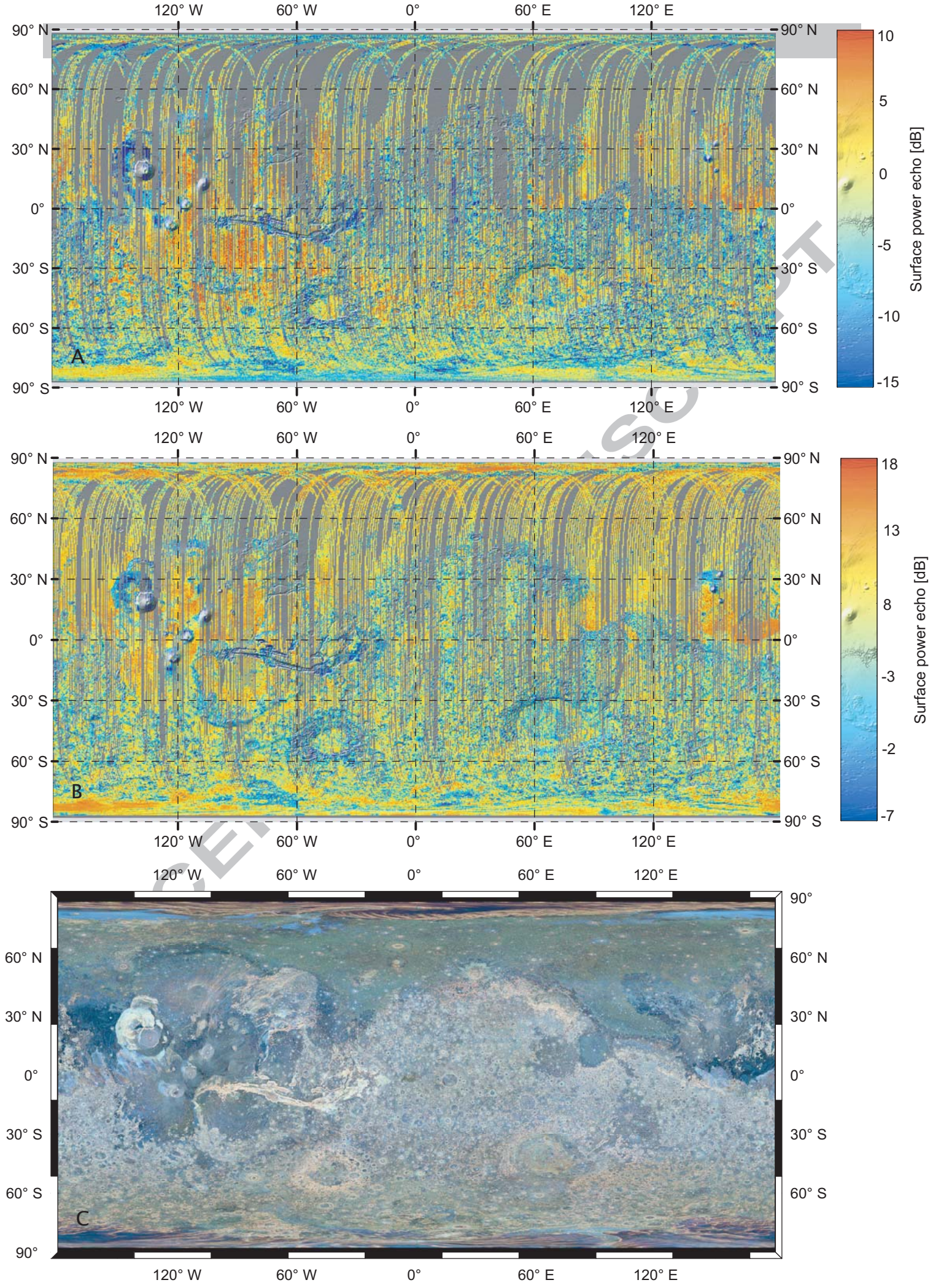
120° W
60° W
0°
60° E
120° E
90° N
60° N
30° N
0°
30° S
60° S
90° S
A
10
5
0
-5
-10
-15
Surface power echo [dB]
B
18
13
8
-3
-2
-7
Surface power echo [dB]
C


50 m

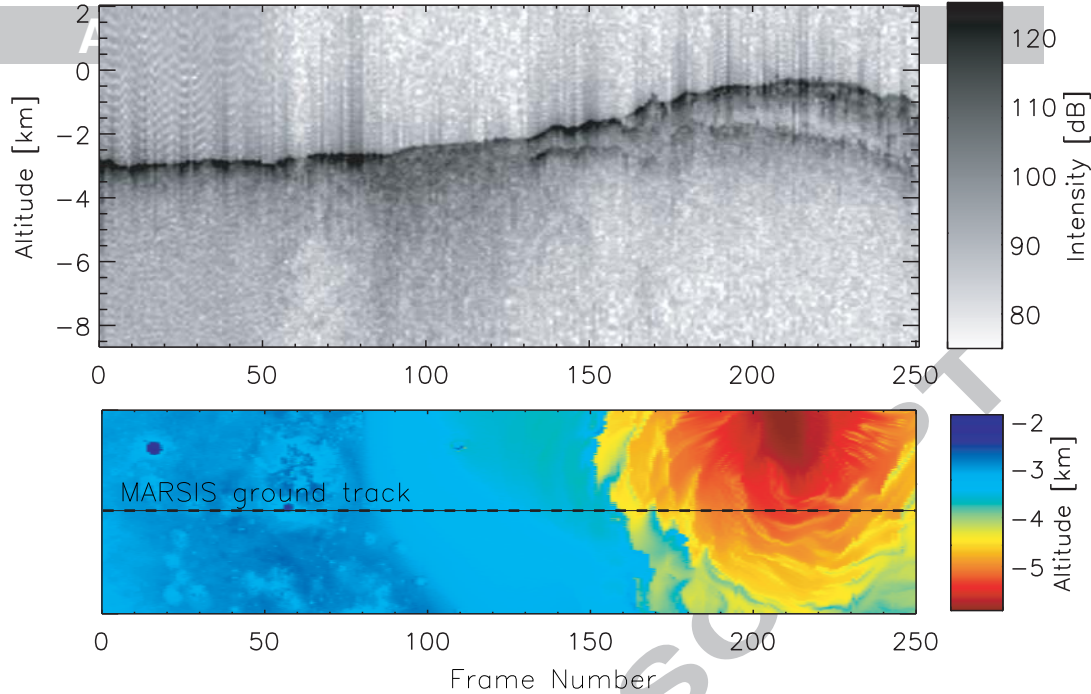
Altitude [km]
2
0
−2
−4
−6
−8
0
50
100
150
200
250
120
110
100
90
80
Intensity [dB]
MARSIS ground track
−2
−3
−4
−5
Altitude [km]
Frame Number

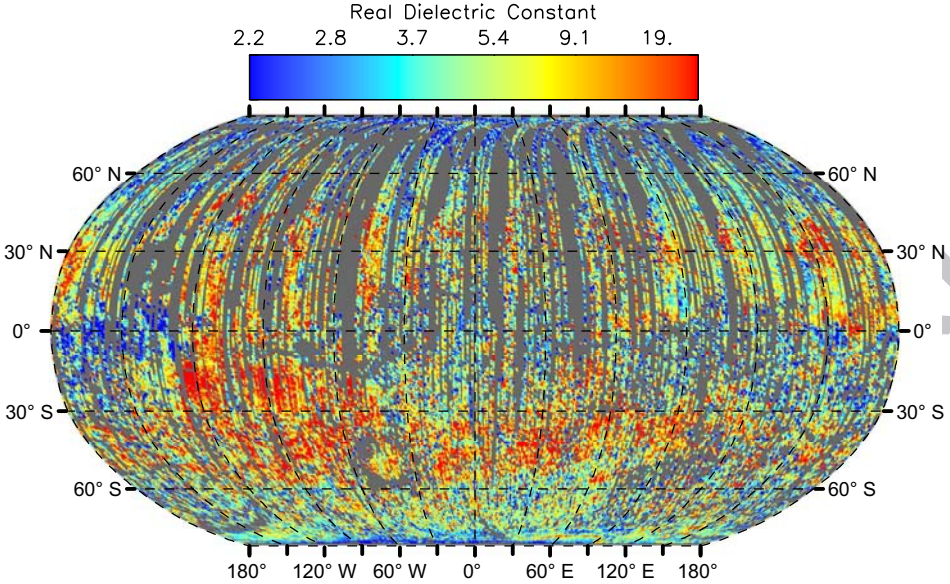

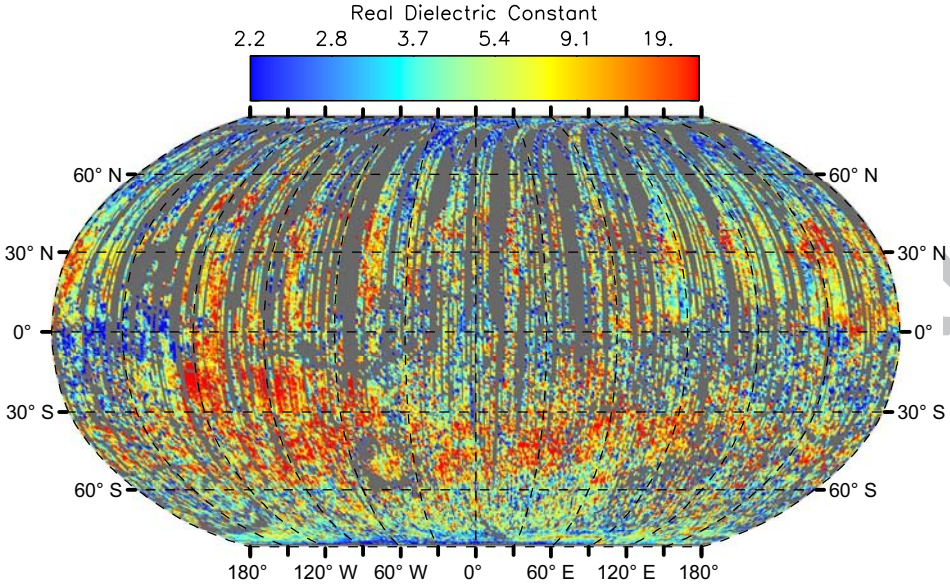

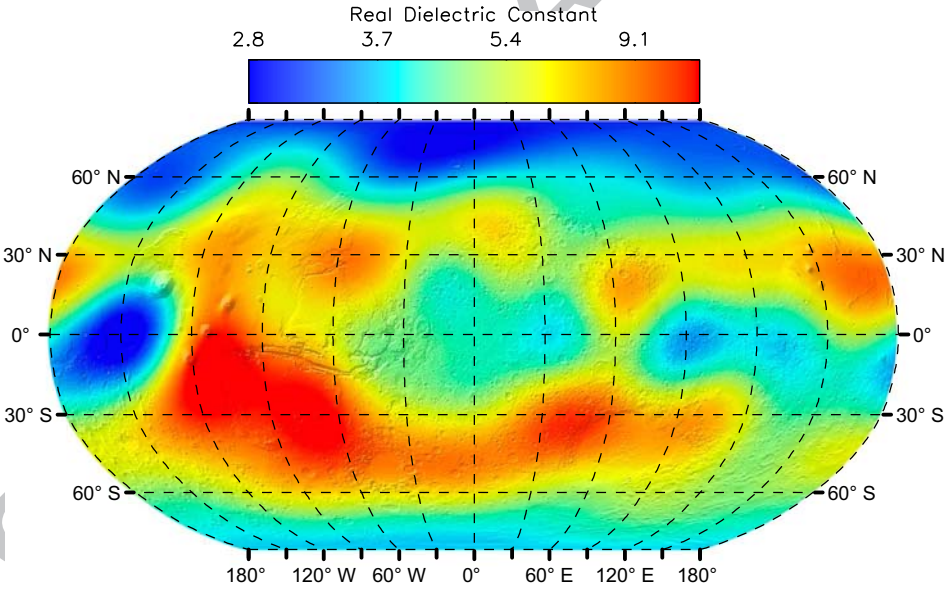

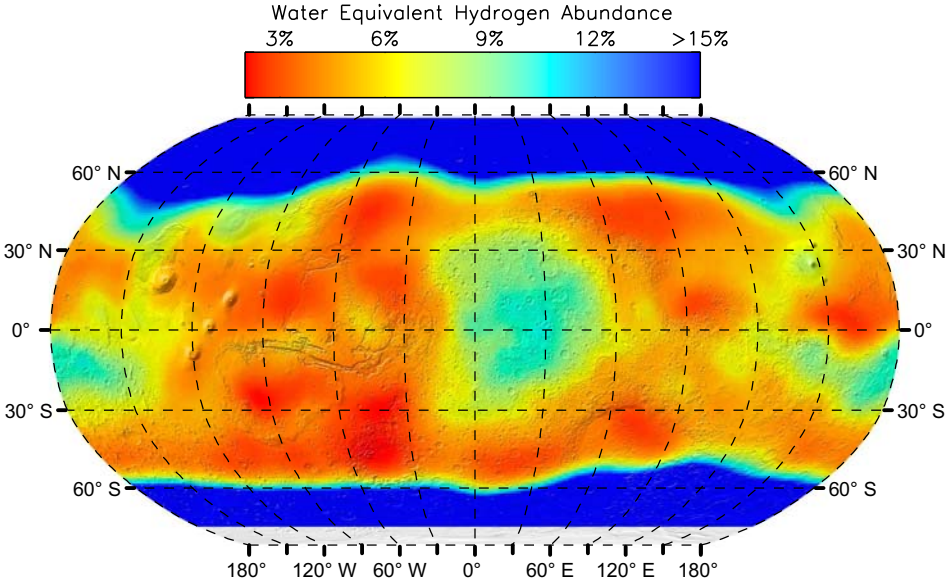

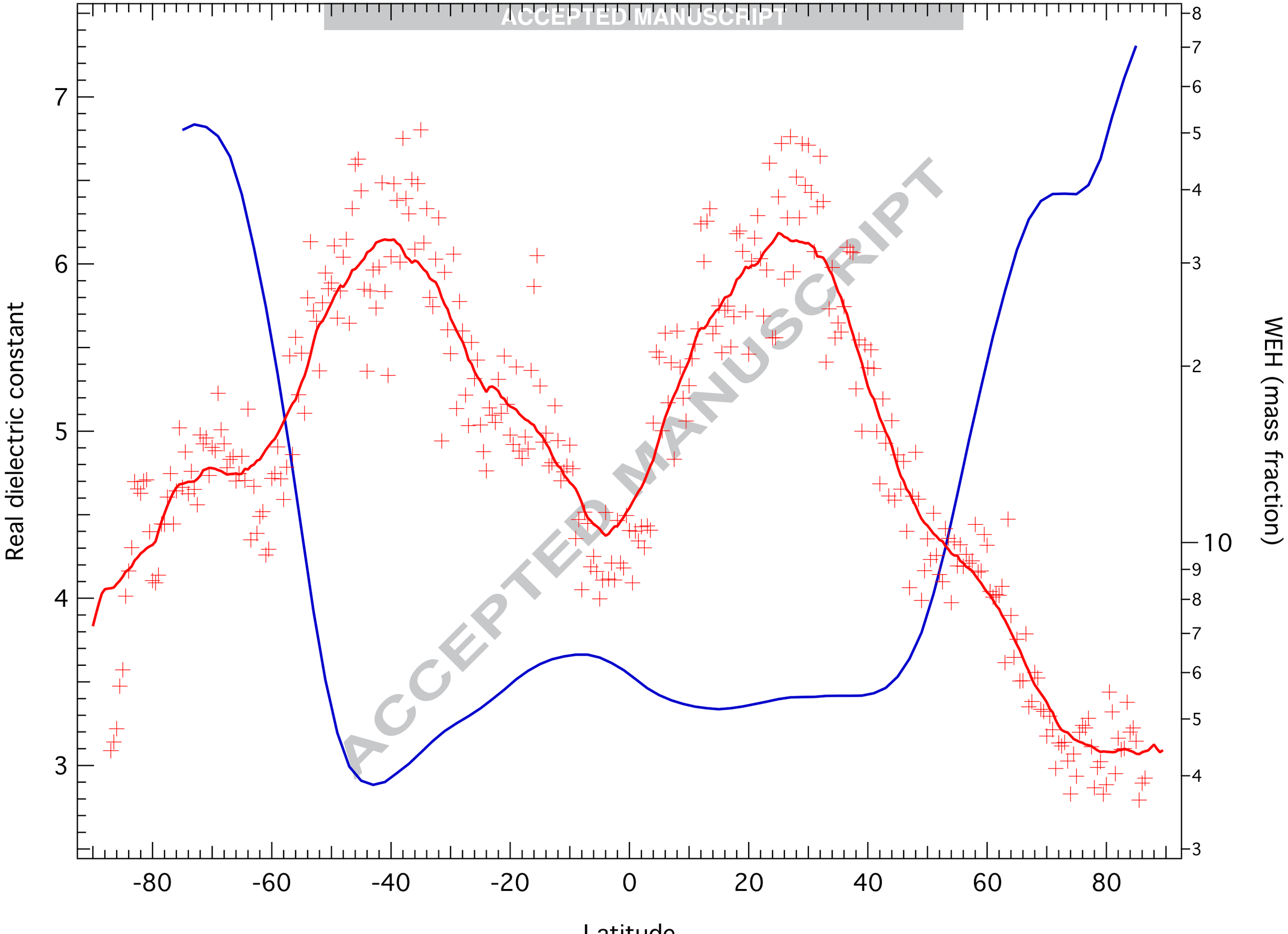

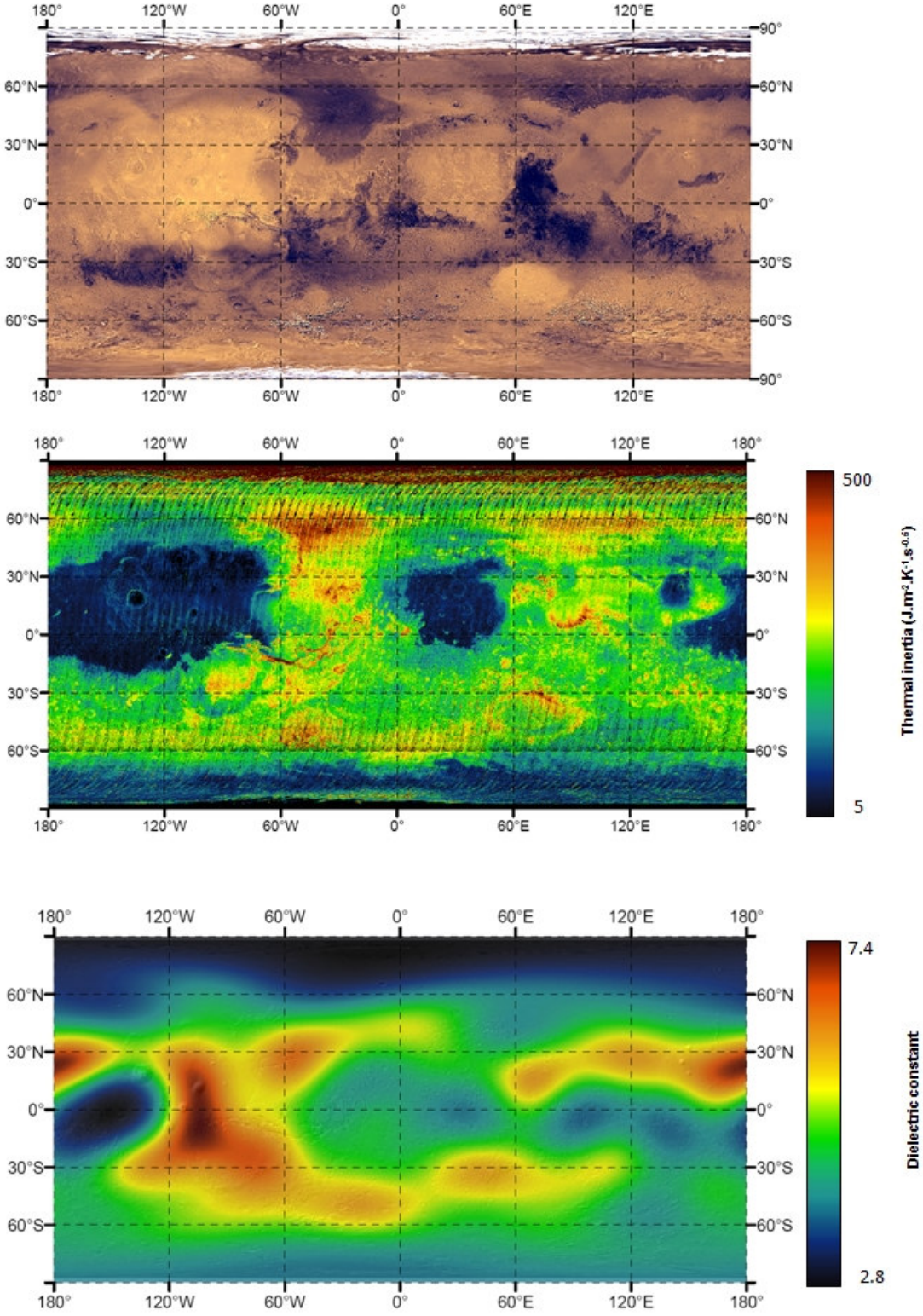

Elsevier Editorial System(tm) for Icarus
Manuscript Draft

Manuscript Number: ICARUS-11322R3

Title: The 3-5 MHz global reflectivity map of Mars by MARSIS/Mars Express: implications for the current inventory of subsurface H2O.

Article Type: Regular Article

Keywords: Mars, surface
Radar observations
Data reduction techniques

Corresponding Author: Dr. Jeremie Mouginot, Ph.D.

Corresponding Author's Institution: University of California

First Author: Jeremie Mouginot, Doctor

Order of Authors: Jeremie Mouginot, Doctor; Antoine Pommerol; Wlodek Kofman; Pierre Beck; Bernard Schmitt; Cyril Grima; Alain Herique; Ali Safaeinili; Jeffrey J Plaut

Abstract: We extracted the surface echo power from two years of MARSIS measurements. The retrieved values are calibrated to compensate for changes in the distance of the spacecraft to the surface and for the attenuation of the signal by the ionosphere. The results are used to build the first global map of surface echo power at 3-5 MHz. The surface echo power variations are primarily caused by km-scale surface roughness. Then, we derive the values of dielectric constant of the shallow subsurface materials by normalizing the surface echo power map using a simulation of MARSIS signal from the MOLA topography. As a result, we obtain a map that characterizes the dielectric properties of the materials down to a few decameters below the surface. Dielectric properties vary with latitude, with high values in mid-latitudes belts (20-40°) and lower values at both equatorial and high latitudes. From the comparison of MARSIS reflectivity map to GRS observations, we conclude that the reflectivity decrease observed poleward of 50-60° corresponds to the onset of water-ice occurrence within the regolith. Assuming homogenous ground composition and texture at the scale of the MARSIS resolution cell, our inferred volume of ground water ice is of 106 km3, equivalent to a polar cap. Low reflectivity areas are also observed in equatorial regions. From radar studies alone, equatorial low dielectric constant values could have different interpretations but the correlation with GRS hydrogen distribution rather points toward a water related explanation.